



Long Island Sound Temperature Variability and its Associations with the Ridge-trough Dipole and Tropical Modes of Sea Surface Temperature Variability

Justin A. Schulte¹, Sukyoung Lee²

5 ¹Davidson Laboratory, Stevens Institute of Technology Hoboken, New Jersey, 07030, United States

²Department of Meteorology, The Pennsylvania State University, University Park, 16823, United States

Correspondence to: Justin A. Schulte (jschulte12@yahoo.com)

Abstract. Possible mechanisms behind the longevity of intense Long Island Sound (LIS) water temperature events are examined using an event-based approach. By decomposing a LIS surface water temperature time series into negative and positive events, it is revealed that the most intense LIS water temperature event in the 1979-2013 period occurred around 2012, coinciding with the 2012 ocean heat wave across the mid-Atlantic Bight. The LIS events are related to a ridge-trough dipole pattern whose strength and evolution can be measured using a dipole index. The dipole index was shown to be strongly correlated with LIS water temperature anomalies, explaining close to 64% of cool-season LIS water temperature variability. Consistently, a major dipole pattern event coincided with the intense 2012 LIS warm event. A composite analysis revealed that long-lived intense LIS water temperature events are associated with tropical sea surface temperature (SST) patterns. The onset and mature phases of LIS cold events were shown to coincide with central Pacific El Niño events, whereas the termination of LIS cold events was shown to possibly coincide with canonical El Niño events or El Niño events that are a mixture of eastern and central Pacific El Niño flavors. The mature phase of LIS warm events was shown to be associated with negative SST anomalies across the central equatorial Pacific, though the results were not found to be robust. The dipole pattern was also shown to be related to tropical SST patterns and fluctuations in central Pacific SST anomalies were shown to evolve coherently with the dipole pattern and the strongly related East Pacific/North Pacific pattern on decadal time scales. The results from this study have important implications for seasonal and decadal prediction of the LIS thermal system.



1 Introduction

Fluctuations in sea surface temperature (SST) across coastal portions of the United States (U.S) are driven by changes in oceanic and atmospheric circulation patterns. Changes in water temperature along the U.S west coast are related to the Pacific Decadal Oscillation (PDO) and the North Pacific Gyre Oscillation, as well-documented by numerous studies (Mantua et al., 1997, Mantua and Hare, 2002, Di Lorenzo, 2008). For the U.S east coast, water temperature fluctuations are related to changes in the Gulf Stream position and variations in the Atlantic Multidecadal Oscillation, PDO, and East Pacific/North Pacific (EP/NP) pattern (Pershing et al., 2015, Schulte et al., 2017). Superimposed on the water temperature changes driven by natural modes of variability is background warming associated with anthropogenic climate change (Pershing et al., 2015).

Although the mechanisms behind SST variability along the U.S west coast are well-documented, comparatively fewer studies have focused on understanding SST variability across the mid-Atlantic Bight in the context of large-scale climate modes. Two recent studies put water temperature variability across the Gulf of Maine and the Long Island Sound (LIS) in a climate-mode context. The first study by Pershing et al. (2015) showed that the combination of Gulf Stream and PDO influences led to rapid warming of the Gulf of Maine that resulted in the collapse of the cod fishery. Because of the PDO and Gulf Stream influences, SST trends across the Gulf of Maine are large compared to SST trends across other regions of the world. More recently, the second study by Schulte et al. (2017) found the EP/NP pattern to be a dominant pattern governing LIS water temperature variability. The EP/NP pattern was shown to have strong decadal variability, and the decadal component of the EP/NP pattern was termed the quasi-decadal mode (Schulte et al. 2017). This quasi-decadal mode was shown to fluctuate coherently with LIS water temperature anomalies. The physical mechanism contributing to the EP/NP decadal variability was not identified, underscoring the need for an additional study that can identify a possible source of the EP/NP decadal variability. Understanding the mechanisms behind the EP/NP decadal variability has implications for seasonal and decadal prediction of LIS water temperature.

Although the LIS is located adjacent to the Atlantic Ocean, LIS water temperature variability is neither strongly related to changes in the Gulf Stream position nor fluctuations in the North Atlantic Oscillation (NAO; Hurrell, 1995). The weak Gulf Stream influence is likely the result of the LIS being a



semi-enclosed water basin. The general movement of weather systems from west to east may reflect the weak NAO influences because the NAO's centers of action are located downstream of the LIS. The weak Gulf Stream and NAO associations with LIS water temperature suggest that an improved understanding of LIS water temperature variability may be obtained by better understanding how climate patterns located upstream from the LIS can impact LIS water temperature. Given that tropical SST patterns can modulate the frequency of occurrence of teleconnection patterns whose centers of action are located upstream of the LIS (e.g. Pacific-North American Pattern (PNA); Svoma, 2011), an additional study is needed to identify possible relationships between LIS water temperature variability and tropical SST patterns.

10 In this paper, we use an event-based approach to identify LIS water temperature relationships with atmospheric and oceanic patterns. More specifically, the main objectives of the study are the following: (1) identify the atmospheric and tropical SST patterns associated with LIS water temperature events; (2) create a simple atmospheric index that is strongly correlated with LIS water temperature variability; and (3) use the simple atmospheric index to better understand LIS water temperature variability.

15 **2 Data**

In this paper, SST fields from 1870 to 2013 are based on the Hadley Centre Global Sea Ice and Sea Surface Temperature (HadISST1) data set (Rayner et al., 2016). Atmospheric fields were analyzed using 500-hPa geopotential height fields based on the National Oceanic Atmospheric Administration's 20th century reanalysis (Compo et al., 2011) and the National Center for Atmospheric Prediction (NCEP; 20 Kalnay et al., 1996) reanalysis. The 20th century reanalysis data product was used because the data set extends back to 1851, whereas NCEP reanalysis data only extend back to 1948. Mean monthly air temperature data from 1979 to 2013 were based on the observed U.S climate divisional data set (Guttman and Quayle, 1996). The data set comprises average monthly temperature data for 344 climate regions (Figure 1a) that partition the U.S into homogeneous climate zones. The annual cycles were removed from 25 the data by subtracting the mean monthly values for each month from the monthly values of the corresponding month for each grid point or climate division.



LIS surface water temperature data used in this study were generated from the New York Harbor Observing Prediction System (NYOPS; Georgas et al., 2016) model. The NYHOPS model is a three-dimensional hydrodynamic model with 11 vertical levels. Following Schulte et al. (2017), water temperature computed on the 1st vertical level was considered surface water temperature. To obtain a single time series representing LIS surface water temperature (for brevity, referred to as LIS temperature, hereafter), water temperature was averaged over the gray-shaded region shown in Figure 1b. The annual cycle in the resulting LIS temperature time series was removed using 1979-2013 monthly means.

The LIS temperature time series and the SST fields were detrended to remove the long-term trend. The time series were detrended by fitting a least-square fit of a line to the time series and subtracting the line from the time series. To check the sensitivity of results to detrending, the analyses were conducted using both the detrended and non-detrended data. Results for the detrended analysis are shown unless otherwise specified. The reason for showing the detrended results is that the study is focused on interannual variability rather than long-term trends.

Indices for the NAO (Hurrell, 1995), Arctic Oscillation (AO; Thompson and Wallace, 1998), EP/NP, PNA (Wallace and Gutzler, 1981), and the West Pacific (WP; Barston and Livezey, 1987; Linkin and Nigam, 2008) were obtained from the Climate Prediction Center (CPC). The indices were based on the 1979-2013 period. The NAO, WP, PNA, and EP/NP indices obtained from the CPC were calculated from a rotated principal component analysis (RPCA) of 500-hPa geopotential height anomalies poleward of 20°N. The AO index was calculated from a rotated RPCA analysis of 1000-hPa geopotential height anomalies. Data for the 1950-2013 period was also used for the EP/NP index.

The Niño 3 and Niño 4 indices from 1870 to 2013 (available at https://www.esrl.noaa.gov/psd/gcos_wgsp/Timeseries/) were used to measure the strength and evolution of the El-Niño/Southern Oscillation (ENSO). Whereas the Niño 3 index better describes the evolution of canonical ENSO, the Niño 4 index better describes the evolution of central Pacific ENSO events (Kao and Yu, 2009; Lee and McPhaden, 2010) Thus, using these two indices, we accounted for two different flavors of ENSO. The annual cycles from these ENSO metrics were removed using the long-term (1870-2013) monthly means.



3 Methods

3.1 Event Decomposition

To better understand the characteristics of climate time series, time series were decomposed into negative and positive events. More specifically, let a time series X be a sequence of N data points x_1, x_2, \dots, x_N at the time points t_1, t_2, \dots, t_N , where the data points were assumed to be equally spaced. Data points were based on monthly anomalies so that they were both positively and negatively valued. Thus, a complete sequence x_1, x_2, \dots, x_N was partitioned into subsequences comprising adjacent data points whose values are of similar sign. Such subsequences were termed positive or negative events depending on the values of the data points.

The onset and decay of events were defined as follows. A negative event E_{neg} was said to begin at t_j if $x_j < 0$ and $x_{j-1} > 0$. A negative event beginning at t_j was said to terminate at $t_k \geq t_j$ if $x_k < 0$, $x_{k+1} > 0$, and $x_i < 0$ for all i such that $j \leq i \leq k$. A similar definition was used to define positive events, but the sign conventions were reversed. The time point t_j was termed the onset phase and the time point t_k was termed the decay phase. The peak intensity of a negative (positive) event was deemed the minimum (maximum) value obtained by a data point within the event period $[t_j t_k]$. If the peak intensity of an event occurred at t_p , then t_p was termed the mature phase.

Given this definition of an event, an event occurring over the time period $[t_j t_k]$ contained $M = t_k - t_j + 1$ data points, where the integer M was regarded as the persistence of the event. The cumulative intensity (referred to as the intensity, hereafter) of an event E was defined as

$$I = \sum_{i=1}^M y_i, \quad (1)$$

where the y_i are data points composing the event E . The absolute value of intensity was deemed the magnitude of an event. Two data points can have identical values but belong to events with very different intensities. The intensity metric, therefore, was useful for differentiating features in the examined time series.

The duration and intensity of events were depicted using an event spectrum. The event spectrum was comprised of line segments beginning at the onset phases and ending at the termination phases of the



events. That is, for each event, a line segment was drawn from the point (t_j, I) to the point (t_k, I) so that the length of the line segment represented the event duration.

3.2 Wavelet Analysis

To extract time-frequency information from a time series X , a wavelet analysis (Torrence and Compo, 1998) was implemented. The wavelet transform of X is given by

$$W_n^X(s) = \sqrt{\frac{2\delta t}{s}} \sum_{n'=1}^N x_{n'} \psi^* \left[\frac{(n'-n)\delta t}{s} \right], \quad (2)$$

where ψ is the Morlet wavelet given by

$$\psi(\eta) = \pi^{-1/4} e^{i\omega_0\eta} e^{-\frac{1}{2}\eta^2}, \quad (3)$$

$\omega_0 = 6$ is the dimensionless frequency, t is time, s is wavelet scale, δt is a time step (1 month in this study), $\eta = s \cdot t$, and the asterisk denotes the complex conjugate (Torrence and Compo, 1998).

To quantify the relationships between climate modes and water temperature as a function of frequency and time, a wavelet coherence analysis was conducted. Following Grinsted et al. (2004), the (local) wavelet squared coherence between two time series X and Y is given by

$$R_n^2(s) = \frac{|S(s^{-1}W_n^{XY}(s))|^2}{S(s^{-1}|W_n^X(s)|^2) \cdot S(s^{-1}|W_n^Y(s)|^2)}, \quad (4)$$

where $W_n^{XY}(s)$ is the cross-wavelet transform defined as the product of the wavelet transform of X and the complex conjugate of the wavelet transform of Y . In Eq. (4), S is a smoothing operator that smooths coherence in time and in wavelet scale (Grinsted et al., 2004). Using Monte Carlo methods, the statistical significance of wavelet squared coherence was assessed by generating 10000 pairs of surrogate red-noise time series with the same lag-1 autocorrelation coefficients as the input time series and computing the wavelet squared coherence between each pair (Grinsted et al., 2004).

To reduce the number of false positive results arising from the simultaneous testing of multiple hypotheses (Maraun and Kurths, 2004; Maraun et al., 2007; Schulte et al., 2015; Schulte, 2016), the cumulative area-wise test developed by Schulte (2016) was applied. The test tracked how the areas of contiguous regions of pointwise significance (significance patches) changed as the pointwise significance level was altered. The test was applied by computing the normalized areas of pointwise significance patches over a discrete set of pointwise significance levels. The normalized area of a patch was defined



as the patch area divided by the square of its centroid's scale coordinate (Schulte et al., 2015; Schulte, 2016). In this study, the normalized areas were computed using pointwise significance levels ranging from $\alpha = 0.02$ to $\alpha = 0.18$. The spacing between adjacent pointwise significance levels was set to 0.02.

The strength of coherence was also measured using global coherence (Schulte et al., 2016), the time-averaged representation of local wavelet squared coherence. Global coherence is given by

$$G_C(s) = \frac{|W^{XY}(s)|^2}{\left(\sum_{n=1}^N |W_n^X(s)|^2\right)\left(\sum_{n=1}^N |W_n^Y(s)|^2\right)}, \quad (6)$$

where

$$W^{XY}(s) = \sum_{n=1}^N W_n^X(s)W_n^{Y*}(s). \quad (7)$$

(Schulte et al., 2016). The statistical pointwise significance of $G_C(s)$ was computed using Monte Carlo methods in a similar manner to local wavelet squared coherence.

A lower dimensional version of the cumulative area-wise test was applied to the global coherence spectra to reduce the number of false positive results (Schulte et al., 2017). The test assessed the statistical significance of one-dimensional. Arc length is an integrated metric accounting for the width of the peak in wavelet scale (frequency) and the extent to which the peak is above the critical level of the pointwise test. To track how the arc length of a given pointwise significance peak changed as the pointwise significance level was altered, the arc length of the pointwise significance peak was computed at pointwise significance levels ranging from 0.02 to 0.18. The test statistic in this case is cumulative arc length. Normalized arc lengths were used to account for how peaks widen with wavelet scale. This normalization was achieved by computing the logarithm (base 2) of the wavelet scales. To further normalize, global coherence values at each wavelet scale were divided by the critical level of the test associated with the pointwise significance level 0.02 at each wavelet scale. The null distribution for the cumulative arcwise test was obtained by generating surrogate red-noise timeseries in the same manner as the cumulative area-wise test. For reference, we also plotted the traditional 5% pointwise significance bounds on all global spectra plots in this study. The reader is referred to Schulte et al. (2017) for more details regarding the cumulative arcwise test.



4 Results

4.1 LIS Temperature Time Series

5 The time series of detrended LIS temperature anomalies is shown in Figure 2. Some notable features are the cool period around 1982 and the warm event around 2012. The 1982 cool period is rather intense, with LIS temperature anomalies approaching -2°C . In contrast, the 2012 event is associated with a maximum temperature anomaly of approximately 4°C , making this water temperature anomaly the largest in the 1979-2013 period. Other prominent features include the cool periods around 1996 and 2003
10 and the warm events around 1991 and 2001. The 1990's is a generally cold period associated with negative LIS temperature anomalies routinely reaching -1.5°C .

To better understand the time series shown in Figure 2a, the time series was decomposed into events to construct the event spectrum shown in Figure 2b. As shown in Figure 2b, both the cool period around 1982 and the warm episode around 2012 are both, respectively, the most intense cool and warm
15 events in the 1979-2013 period. Other prominent cold events are shown to have occurred around 1996, 2003, and 2011. The 1996 and 2003 cold events are nearly as intense as the 1982 event (Table 1). The two most intense warm events are the 1991, 2001, and 2012 warm events. The magnitude of the 2012 warm event far exceeds that of any other event despite the removal of the long-term trend. This result suggests that atmospheric variability may have contributed strongly to that event.

20 4.2 LIS Events and Atmospheric Patterns

To diagnose a possible mechanism behind the occurrence of the intense LIS events, the correlation between 500-hPa geopotential height anomalies and detrended LIS temperature anomalies was conducted. For this analysis, we focused on the December-February (DJF) season because atmospheric circulation anomalies are generally most pronounced during the DJF season.

25 Shown in Figure 3 is the correlation between DJF LIS temperature anomalies and 500-hPa geopotential height anomalies. The positive correlation between LIS temperature anomalies and 500-hPa geopotential height anomalies over the eastern U.S suggest that warmer-than-normal LIS temperature



conditions are associated with a jet stream ridge, which is consistent with how jet stream configurations can influence the temperature in the coastal ocean off the northeastern U.S (Chen et al., 2014). Similarly, the negative correlations with 500-hPa geopotential height anomalies across Alaska indicate that LIS warm events are associated with an anomalous trough over Alaska. Thus, it appears that LIS temperature events are related to a ridge-trough dipole pattern, an anomalously amplified wave pattern across the U.S.

To better understand LIS water temperature variability, a ridge-trough dipole index was created based on the pattern identified in Figure 3. The dipole index was constructed by first locating the grid point for which the correlation between LIS temperature and 500-hPa geopotential height anomalies is minimum. This grid point is located at 70°N and 157.5°W and is marked by a cyan cross in Figure 3. Next, the grid point for which the correlation between LIS temperature and 500-hPa geopotential height anomalies is maximum was located. This grid point is located at 42.5°N and 75°W and is marked with a magenta cross in Figure 3. Following Wang et al. (2014), the dipole index for a given month was defined as the 500-hPa geopotential height anomaly at 42.5°N and 75°W minus the 500-hPa geopotential height anomaly at 70°N and 157.5°W. Thus, the dipole index measures the intensity of the ridge-trough dipole pattern such that positive phases generally indicate that an anomalously strong ridge over the eastern U.S is accompanied by an anomalous trough over Alaska.

The time series for the dipole index is shown in Figure 4a. The time series is rather noisy, but notable features can still be identified without any filtering. The dipole pattern, as indicated by positive dipole indices, is seen to be in a persistent positive phase around the 2012 LIS warm event. Other features of the dipole index are more readily discernable from an inspection of the event spectrum shown in Figure 4b. According to the event spectrum, the positive dipole event around 2012 is quite intense but not as intense as the 1882 positive dipole event that persists for 11 months (Table 2). The most intense negative dipole event occurs around 1977. A comparison of Tables 1 and 2 shows that the second most intense negative dipole event coincides with the second most intense LIS cold event that occurred around 2003 (Table 1).

Although a comparison of Tables 1 and 2 shows that the 2012 LIS warm event coincides with the third most intense positive dipole event, the relationship strength between LIS temperature anomalies and the dipole pattern cannot be inferred. How strongly related is the dipole index to LIS water temperature



anomalies? To assess the strength of the dipole index relationship with LIS water temperature anomalies, seasonally averaged detrended LIS temperature anomalies were correlated with the seasonally averaged dipole index. As shown in Figure 5, the dipole index is strongly correlated with LIS temperature anomalies for the October-December (OND), November-January (NDJ), DJF, and January-March (JFM) seasons. The relationships are generally stronger if the dipole index leads by 1 month, as indicated by the dotted line in Figure 5. The lagged correlation coefficients approach 0.8 for the DJF season, suggesting that DJF LIS temperature anomalies are strongly influenced by the dipole pattern in the NDJ season. Lagged correlations are also strong ($r > 0.7$) for the OND, NDJ, and JFM seasons. The relationships are generally weaker in the warm seasons possibly because teleconnection patterns are generally of the weakest amplitude in the warm season.

The relationship strength found between the dipole index and LIS temperature anomalies is consistent with results found in prior work. For example, the dipole index is strongly correlated with the EP/NP index for most months (Table 3) in agreement with how the EP/NP index is strongly correlated with LIS temperature anomalies (Schulte et al., 2017). In contrast, the dipole index is well-correlated with indices for the AO and NAO even though the NAO and AO indices are only weakly correlated with LIS temperature anomalies (Schulte et al., 2017). The dipole index is also correlated with the PNA and WP indices for some warm-season months. The fact that the dipole index is correlated with multiple large-scale indices suggests that the dipole pattern falls on a continuum of teleconnection patterns (Franzke and Feldstein, 2005) such that the dipole pattern is strongly EP/NP-like. While we found by conducting our own EOF analysis of 500-hPa geopotential height anomalies that the AO pattern is the leading mode of variability, the EP/NP pattern appears to be consistently the 5th to 7th leading mode of variability. Thus, although the EP/NP pattern is not as dominant as the AO pattern, the dipole pattern tends to more closely resemble it than the AO pattern.

Given that LIS water temperature is strongly correlated with air temperature (Schulte et al., 2017), it is hypothesized that the dipole index is related to air temperature across the U.S, especially around the LIS. To confirm a dipole index-air temperature relationship, the dipole index was correlated with average monthly air temperature anomalies for the 1979-2013 period (Figure 6). The results for the NDJ season



are only displayed because the NDJ dipole index is most strongly correlated with LIS water temperature anomalies after accounting for lags (Figure 5).

As shown in Figure 6, the dipole index is, indeed, strongly correlated with air temperature anomalies across a large region of the U.S. Correlation coefficients exceed 0.8 and approach 0.9 across the Northeast U.S and LIS region. The strong relationships extend to the southern U.S, and the relationship strengths generally weaken equatorward. The results for the other seasons are similar, but the relationships are generally weaker than those identified for the NDJ season. This result suggests that the dipole pattern may be most dominant in the winter. The strong relationship between the dipole index and U.S air temperature anomalies is consistent with how the intense 2012 dipole event coincides with the record warm March 2012 (Dole et al., 2014), which resulted in a so-called false spring in which plants bloomed prematurely making them susceptible to drought and freezes (Ault, 2013). The results shown in Figure 6 suggest that the dipole pattern's impact on LIS temperature is related to the dipole pattern's influence on air temperature.

4.3 Intense LIS Events and SST Patterns

SST patterns are often used in seasonal forecasting and, thus, identifying an SST pattern precursor to LIS events has implications for seasonal prediction of LIS temperature anomalies. To identify SST patterns associated with LIS temperature events, a lagged SST composite analysis was conducted using detrended LIS warm and cool events separately. The SST composite plots for the warm events were constructed using the LIS warm events whose intensities are greater than or equal to the 50th percentile of all warm event intensities. Similarly, the SST composite plots for the cold events were constructed using LIS cold events whose intensities are less than or equal to the 50th percentile of all LIS cold event intensities. The composite mean SST patterns were computed at the onset, mature, and decay phases of the LIS events.

The results for the LIS cold events are shown in Figure 7. The composite plot shown in Figure 7a indicates that the onset of LIS cold events is associated with positive SST anomalies across the central equatorial Pacific. The results suggest that LIS cold events could be initiated by central Pacific El Niño events (Lee and McPhaden, 2010). El Niño events that have been classified as central Pacific El Niño events are the 1991–92, 1994–95, 2002–03, 2004–05, and 2009–2010 events. The 1991–1992, 2002–2003,



2004-2005, and 2009-2010 events all appear to occur around LIS cold periods (Figure 2a). Note that there could be lags between the onset of central Pacific El Niños and LIS temperature anomalies because of the lagged response of water temperature to atmospheric forcing (Schulte et al., 2017). In addition, pre-existing positive water temperature anomalies may need time to degrade.

5 The SST anomaly pattern for the mature phases of LIS cold events features positive SST anomalies across the central equatorial Pacific (Figure 7b). However, the mature-phase composite mean SST anomaly pattern is more pronounced across the North Pacific Ocean than it is for the onset phase. A region of positive SST anomalies is seen to be horseshoe-shaped, with positive SST anomalies extending from the central equatorial Pacific to the U.S west coast. This horseshoe-shaped anomaly pattern has been shown to be associated with the first three leading modes of Pacific Ocean SST variability (Hartmann, 2015). In particular, the SST pattern shown in Figure 7b resembles the third leading mode of SST variability that tends to precede El Niño events (Hartmann 2015). The pattern shown in Figure 7b is similar to the DJF SST pattern of 1996, which is consistent with how 1996 was a cooler-than-normal period for much of the U.S (Haplert and Bell, 1997) and the LIS (Table 1). Unlike the composite mean SST pattern corresponding to the onset phase, negative SST anomalies are present along the U.S east coast and across the Gulf of Mexico. These results are consistent with how LIS temperature anomalies are strongly associated with the dipole pattern that influences air temperature across regions adjacent to the Gulf of Mexico and U.S east coast. It is likely that the dipole pattern's influence on air temperature extends across coastal waters, resulting in the dipole index being correlated with SST anomalies across the Gulf of Mexico and U.S east coast. This relationship between the dipole index and SST anomalies was confirmed by correlating the dipole index with SST anomalies for different seasons (not shown).

15 The tropical SST pattern associated with the decay phase of LIS cold events is different from those associated with the onset and mature phases (Figure 7c). The composite mean SST anomaly pattern most closely resembles the first leading mode of SST variability called the canonical ENSO pattern (Hartmann, 2015), though the most intense positive SST anomalies are still confined to the central equatorial Pacific. This result suggests that there may be a tendency for the decay of LIS cold events to coincide with canonical ENSO patterns or a SST pattern that is a mixture of central and eastern Pacific El Niños lying on a continuum of ENSO flavors (Johnson, 2013).



The tendency for the decay of LIS cold events to coincide with canonical ENSO patterns is more evident when constructing SST composites using one standard deviation (Figure 8) instead of the 50th percentile used to construct the composite shown in Figure 7c. However, possibly because of small sample sizes, the results generally lack statistical significance. Nonetheless, the event spectrum depicted in Figure 5 2b indicates that the major cool period around 1982, for example, terminates around the major 1982/83 El Niño event (Ramusson and Wallace, 1983), which featured warmer-than-normal winter conditions across the eastern U.S because of relatively weak western U.S jet stream ridging (Quiroz, 1983). Similarly, the 1997/1998 El Niño event (McPhaden, 1999) also coincides with the transition point between cooler-than-normal LIS temperature conditions and warmer-than-normal conditions. The results 10 are also consistent with how the major 2016 El Niño event occurred around the end of a cold period not considered in this study (see Section 5). The results from this study suggest that major El Niño events could mark the end of major LIS cold periods. Physically, major El Niño events could end LIS cold events because of the release of heat into the atmosphere during El Niño events that influences the global mean temperature (Hu and Fedorov, 2017). The results shown in Figure 8 are also consistent with how the SST 15 pattern at mature phases of LIS cold events (Figures 7b and 8b) tends to precede warm ENSO events (Hartmann, 2015).

The composite analysis was also conducted for LIS warm events and the results revealed that LIS warm events are also associated with SST modes of variability (Figure 9). The onset of LIS warm events appears not to be associated with any coherent SST pattern. For the mature phase, negative SST anomalies 20 are seen across the central equatorial Pacific and positive SST anomalies are seen across the eastern equatorial Pacific. Like the SST anomaly pattern associated with mature phases of LIS cold events (Figures 7b and 8b), the pattern shown in Figure 9b generally resembles the 3rd leading mode of SST variability (Hartman, 2015). The SST pattern corresponds well with the SST anomaly pattern associated with March 2012 (not shown), a month in which record warmth was experienced across the central and 25 eastern U.S (Dole et al., 2014). The mature phases are also associated with positive SST anomalies along the U.S east coast and across the Gulf of Mexico. Consistently, March 2012 featured positive SST anomalies across the Gulf of Mexico and along the U.S east coast (Dole et al., 2014). Decay phases



(Figure 9c) appear to be associated with negative SST anomalies across the eastern and central equatorial Pacific, but the results were not found to be statistically significant.

The results for the warm LIS events were found to be sensitive to the threshold used to construct the composites. For example, if we only considered the LIS warm events whose intensities were greater than or equal to the 90th percentile of LIS warm event intensities, then all phases of LIS warm events would resemble the pattern shown in Figure 9b. In general, the positive SST anomalies across the eastern Pacific were found to become more intense as the percentile used to establish the threshold was increased from 50 to 90. Despite the lack of statistical significance in the composite plots, statistically relationships with SST anomalies were found when correlating DJF LIS temperature anomalies with DJF SST anomalies (not shown). The identified correlation pattern was found to strongly resemble the pattern shown in Figures 7b and 8b.

The SST composite analyses were also conducted using the dipole events for the 1979-2013, 1950-2013, and 1870-2013 periods. The resulting SST patterns were found to be like those shown in Figures 7, 8, and 9, which is not surprising given the strong correlation between the dipole index and LIS temperature anomalies. Correlating the DJF dipole index with DJF SST anomalies revealed a correlation pattern matching the pattern shown in Figures 7b, 8b, and 9b (not shown). The results suggest that SST anomalies across the western and central equatorial Pacific are related to the occurrence of dipole events.

4.4 Decadal Variability

The results of the composite analyses suggest that dipole events may be associated with tropical SST patterns, but the time scale at which the SST patterns are most strongly associated with the dipole pattern cannot be inferred. Thus, a wavelet coherence analysis was conducted to determine if the SST modes fluctuate coherently with the dipole pattern at a preferred time scale. The wavelet squared coherence was computed between the dipole index and indices for Niño 3 and Niño 4 metrics, but the results using the Niño 4 index were found to be most robust. As such, the results for the Niño 4 index analysis are only shown.

The results shown in Figure 10 indicate that the dipole and Niño 4 indices fluctuate coherently in the 64- to 128-month period band after 1930 as shown in Figure 10a. The results suggest that stronger decadal-scale fluctuations in central equatorial Pacific SSTs are associated with larger decadal



fluctuations in the dipole pattern. Given that the decadal-scale fluctuations in the dipole pattern contribute to the overall variance of the dipole index around 2012, the decadal-scale fluctuations must contribute to some extent to the intense dipole event of 2012. The results from the coherence analysis thus suggest that central equatorial Pacific SST fluctuations may have contributed to that intense dipole event.

5 The strong correlation between the EP/NP and dipole indices (Table 3) suggests that the coherence between the EP/NP and Niño 4 indices is also strong. The strong coherence was confirmed by computing the wavelet squared coherence between the EP/NP and Niño 4 indices for the 1950-2013 period. To perform the analysis, the missing values for the EP/NP index in December were filled by establishing a linear relationship between the EP/NP and dipole indices for all months but December. The linear
10 relationship was obtained using a least-square fit of a line, and it was used to fill missing EP/NP values based on the available December dipole index values.

As shown in Figure 11, the EP/NP index does, indeed, fluctuate coherently with the Niño 4 index. The coherence appears to be strong, and the global coherence spectrum shows arcwise significant global wavelet coherence in the 64-128 period band. As shown by Schulte et al. (2017), the EP/NP pattern
15 fluctuates strongly on quasi-decadal time scales and, thus, the results shown in Figure 11 suggest that EP/NP variability on quasi-decadal time scales may be related to quasi-decadal fluctuations in central equatorial Pacific SSTs. Schulte et al. (2017) also showed that the EP/NP pattern fluctuates coherently with LIS water temperature on decadal time scales, suggesting that LIS water temperature anomalies may also fluctuate coherently with the Niño 4 index on decadal timescales. The LIS water temperature time
20 series, however, is too short to make such inferences, though the composite analyses shown in Figures 7, 8, and 9 support the hypothesis that central equatorial Pacific and canonical El Niño events are associated with LIS water temperature variability.

5 Conclusion and Discussion

This paper revealed that LIS events are associated with modes of tropical Pacific and North Pacific
25 SST variability. The spatial characteristics of the SST patterns was demonstrated to depend on the phase of the LIS events. The onset of LIS cold events was shown to be associated with central equatorial Pacific SST anomalies, whereas the decay phase of such events was shown to coincide with canonical ENSO



events. These results suggest that central Pacific El Niño events can be used to construct outlooks for the onset of major LIS cold events. Similarly, information regarding the formation of canonical ENSO events could prove useful as guidance for assessing how likely a LIS cold event will end. Conversely, major LIS cold events could be used to anticipate the formation of El Niño events.

5 The strong relationships identified between the dipole index and LIS temperature anomalies suggest that the dipole index should be incorporated into LIS temperature outlooks and possibly temperature outlooks for other regions of the U.S. as well. The forecast skill associated with such outlooks will depend on the ability to predict the phase and intensity of the dipole pattern. The association between tropical SST patterns and the dipole pattern could prove useful in extended dipole pattern outlooks,
10 contrasting with the AO index whose predictability is limited (Jung et al., 2011). The coherence between the Niño 4 index and indices for the EP/NP and dipole patterns supports the idea that extended dipole pattern outlooks based on tropical SST patterns may be possible. More research, however, is needed to quantify the ability of dynamical weather and seasonal forecasting models to predict the pattern.

 Although not the focus of this paper, the dipole pattern may be an important temperature indicator
15 for other estuaries across the Northeast U.S. The correlation pattern shown in Figure 6 suggests that the dipole pattern could be an important temperature indicator for the Delaware Bay and Chesapeake Bay estuaries. The strong correlation between air temperature and the dipole index across Maine also suggests that the dipole pattern may contribute significantly to the variability of water temperature across the Gulf of Maine. The Gulf of Maine has experienced rapid warming during the past decade (Pershing et al.,
20 2015) and understanding the causes of the rapid warming has important implications for fisheries. Future work could therefore include understanding how the dipole pattern may have contributed to the rapid Gulf of Maine warming.

 The results from the present analysis are consistent with temperature events that occurred after the study period considered in this study. For example, the cold period around February 2015 transitioned
25 into a record warm period for most of the U.S. The record warm period lasting from September 2015 to December 2015 coincided with one of the most intense EL Nino events on record. In agreement with our results, the February 2015 SST pattern strongly resembled the SST pattern shown in Figure 7b, which our results suggest occurs at the peak of LIS cold events. Furthermore, the SST pattern and extreme cold



across the eastern US occurred before the EL Nino formation, which is also in agreement with the results from the present study. These recent events support the results from our study that indicate extended LIS temperature outlooks may be possible if information regarding ENSO flavors are incorporated into such outlooks.

5

Data availability

The 20th century reanalysis data is available at https://www.esrl.noaa.gov/psd/data/20thC_Rean/ and
10 NCEP reanalysis data are available at
<https://www.esrl.noaa.gov/psd/data/gridded/data.ncep.reanalysis.html>. The Hadley SST data are
available at <https://www.metoffice.gov.uk/hadobs/hadisst/data/download.html>. Monthly indices for the
atmospheric climate modes can be found at <https://www.esrl.noaa.gov/psd/data/climateindices/list/>, while
the long-term Nino 3.4 and Nino 4 indices are available at
15 https://www.esrl.noaa.gov/psd/gcos_wgsp/Timeseries/. The long island sound data is available at
https://www.researchgate.net/publication/306256135_LIS_tmp_8113.

20



References

- Aman, A. A. and Bman, B. B.: The test article, *J. Sci. Res.*, 12, 135–147, doi:10.1234/56789, 2015.
- Aman, A. A., Cman, C., and Bman, B. B.: More test articles, *J. Adv. Res.*, 35, 13–28, doi:10.2345/67890, 2014.
- 5 Ault, T.R, Henebry, G. M., de Beurs, K. M., Schwartz, M.D., Betancourt, J.L, and Moore, D.: The false spring of 2012, earliest in North American record, *Eos, Trans. Amer. Geophys. Union*, 94, 181–182, doi:10.1002/2013EO200001, 2013.
- Barnston, A., and Livezey, R. E.: Classification, seasonality, and persistence of low-frequency circulation patterns. *Mon. Wea. Rev.*, 115, 1083–1126, 1987.
- 10 Chen, K., Gawarkiewicz, G. G., Lentz, S. J., and Bane, J. M.: Diagnosing the warming of the Northeastern U.S. Coastal Ocean in 2012: A linkage between the atmospheric jet stream variability and ocean response, *J. Geophys. Res. Oceans*, 119, 218–227, doi:10.1002/2013JC009393, 2014.
- 15 Compo, G.P., and co-authors.: The Twentieth Century Reanalysis Project, *Quarterly J. Roy. Meteorol. Soc.*, 137, 1-28, <http://dx.doi.org/10.1002/qj.776>, 2011.
- Di Lorenzo, E., and Coauthors.: North Pacific Gyre Oscillation links ocean climate and ecosystem change, *Geophys. Res. Lett.*, 35, L08607, doi:10.1029/2007GL032838, 2008.
- 20 Franzke, C. and Feldstein, S. B.: The continuum and dynamics of Northern Hemisphere teleconnection patterns, *J. Atmos. Sci.*, 62, 3250–3267, 2005.
- Georgas, N., Yin, L., Jiang, Y., Wang, Y., Howell, P., Saba, V., Schulte, J., Orton, P., and Wen, B.: An open-access, multi-
25 decadal, three-dimensional, hydrodynamic hindcast dataset for the Long Island Sound and New York/New Jersey Harbor Estuaries., *J. Mar. Sci. Eng.*, 4, 48, 2016.
- Grinsted, A., Moore, J. C., and Jevrejeva, S.: Application of the cross wavelet transform and wavelet coherence to geophysical time-series., *Nonlin. Processes Geophys.*, 11, 561-566, 2004.
- 30 Guttman, N. and Quayle, R.: A historical perspective of US climate divisions, *Bull Am Met Soc.*, 77, 293–303, 1996.
- Halpert, M. S. and Bell, G. D.: Climate assessment for 1996, *Bull. Amer. Meteor. Soc.*, 78, S1–S49, 1997.



- Hadley Centre for Climate Prediction and Research/Met Office/Ministry of Defence/United Kingdom. 2000, updated monthly. *Hadley Centre Global Sea Ice and Sea Surface Temperature (HadISST)*. Research Data Archive at the National Center for Atmospheric Research, Computational and Information Systems Laboratory. <http://rda.ucar.edu/datasets/ds277.3/>. Accessed: 12/10/2017.
- 5
- Halpert, M. and Bell, G.: Climate assessment for 1996, *Bull. Amer. Meteor. Soc.*, 78, S1–S49, doi:10.1175/1520-0477(1997)078,1038:CAF.2.0.CO;2, 1997.
- Hartmann, D. L.: Pacific Sea Surface Temperature and the Winter of 2014, *Geophys. Res. Lett.*, 42, 1894–1902, 2015.
- 10
- Hurrell, J. W.: Decadal trends in the North Atlantic Oscillation regional temperatures and precipitation, *Science*, 269, 676–679, 1995.
- Hu, S and Fedorov, A. V.: The extreme El Niño of 2015–2016 and the end of global warming hiatus, *Geophys. Res. Lett.*, 44, 3816–24, 2017.
- 15
- Johnson, N.C.: How Many ENSO Flavors Can We Distinguish?, *J. Climate*, 26, 4816–4827, 2013.
- Jung, T., Vitart, F., Ferranti, L., and Morcrette, J.J: Origin and predictability of the extreme negative NAO winter of 2009/10, *Geophys. Res. Lett.*, 38, L07701, doi:10.1029/2011GL046786, 2011.
- 25
- Kalnay, E., and Coauthors: The NCEP/NCAR 40-year Reanalysis Project, *Bull. Amer. Meteor. Soc.*, 77, 437–472, 1996.
- Kao, H. Y. and Yu, J. Y.: Contrasting eastern-Pacific and central-Pacific types of ENSO, *J. Clim.*, 22, 615– 632, doi:10.1175/2008JCLI2309.1, 2009.
- 30
- Lee, T., and McPhaden, M. J.: Increasing intensity of El Niño in the central-equatorial Pacific, *Geophys. Res. Lett.*, 37, L14603, doi:10.1029/2010GL044007, 2010.
- Linkin, M. E. and Nigam, S.: The North Pacific Oscillation– West Pacific teleconnection pattern: Mature-phase structure and winter impacts, *J. Clim.*, 21, 1979–1997, 2008.
- 35
- Maraun, D. and Kurths, J.: Cross wavelet analysis: significance testing and pitfalls, *Nonlin. Processes Geophys.*, 11, 505-514, 2004.



- Maraun, D., Kurths, J., and Holschneider, M.: Nonstationary Gaussian processes in wavelet domain: synthesis, estimation, and significance testing, *Phys. Rev. E*, 75, doi: 10.1103/PhysRevE.75.016707, 2007.
- 5 Mantua, N. J. and Hare, S. R.: The Pacific decadal oscillation, *J. Oceanogr.*, 58, 35–44, 2002.
- Mantua, N. J., Zhang, Y., Wallace, J. M., and Francis, R. C.: A Pacific interdecadal climate oscillation with impacts on salmon production, *Bull. Amer. Meteor. Soc.*, 78, 1069–1079, 1997.
- 10 McPhaden, M. J.: Genesis and evolution of the 1997–98 El Niño, *Science*, 283, 950–954, 1999.
- Pershing, A. J., and Co-authours, 2015: Slow adaptation in the face of rapid warming leads to collapse of the Gulf of Maine cod fishery, *Science*, 350, 809–812, doi:10.1126/science.aac9819.
- 20 Quiroz, R. S.: The climate of the “El Niño” winter of 1982–83—A season of extraordinary climatic anomalies, *Mon. Wea. Rev.*, 111, 1685–1706, doi:10.1175/1520-0493(1983)111,1685:TCOTNW.2.0.CO;2, 1983.
- Rasmusson, E. M and Wallace, J.M.: Meteorological aspects of the El Niño – Southern Oscillation, *Science*, 222, 1195–1202, 25 1982.
- Rayner, N. A., Brohan, P., Parker, D. E., Folland, C. K., Kennedy, J. J., Vanicek, M., Ansell, T., and Tett, S. F. B.: Improved analyses of changes and uncertainties in sea surface temperature measured in situ since the mid-nineteenth century: the HadSST2 data set., *J. Clim.*, 19, 446–469., 2006.
- 30 Schulte, J. A., Georgas, N., Saba, V., Howell, P.: North Pacific Influences on Long Island Sound Temperature Variability, *J. Clim.*, <https://doi.org/10.1175/JCLI-D-17-0135.1>, 2017.
- Schulte, J. A., Najjar, R.G, and Li, M.: Impacts of Climate Modes on Streamflow in the Mid-Atlantic Region of the United 35 States, *J. Hydrology: Regional Studies*, 5, 80–99, 2016.
- Schulte, J. A.: Cumulative areawise testing in wavelet analysis and its application to geophysical time-series, *Nonlin. Processes Geophys.*, 23, 45–57, 2016.



- Schulte, J. A., Duffy, C., and Najjar, R. G.: Geometric and Topological Approaches to Significance Testing in Wavelet Analysis, *Nonlin. Processes Geophys.*, 22, 139-156, 2015.
- Svoma, B.M.: El Nino–Southern Oscillation and snow level in the western United States, *J. Geophys. Res.*, 116, D24117, doi:10.1029/2011JD016287, 2011.
- Thompson, D. W. J. and Wallace, J. M.: The Arctic Oscillation signature in the wintertime geopotential height and temperature fields, *Geophys. Res. Lett.*, 25, 1297–1300, 1998.
- 10 Torrence, C. and Compo, G. P.: A practical guide to wavelet analysis, *Bull. Amer. Meteor. Soc.*, 79, 61–78, 1998.
- Wallace, J. M. and Gutzler, D. S.: Teleconnections in the geopotential height field during the Northern Hemisphere winter, *Mon. Wea. Rev.*, 109, 784–812, 1981.
- 15 Wang, S.-Y., Hips, L., Gillies, R. R., and Yoon, J. -H.: Probable causes of the abnormal ridge accompanying the 2013–2014 California drought: ENSO precursor and anthropogenic warming footprint, *Geos. Phys. Lett.*, 41, 3220–3226, 2014.

20

25

30

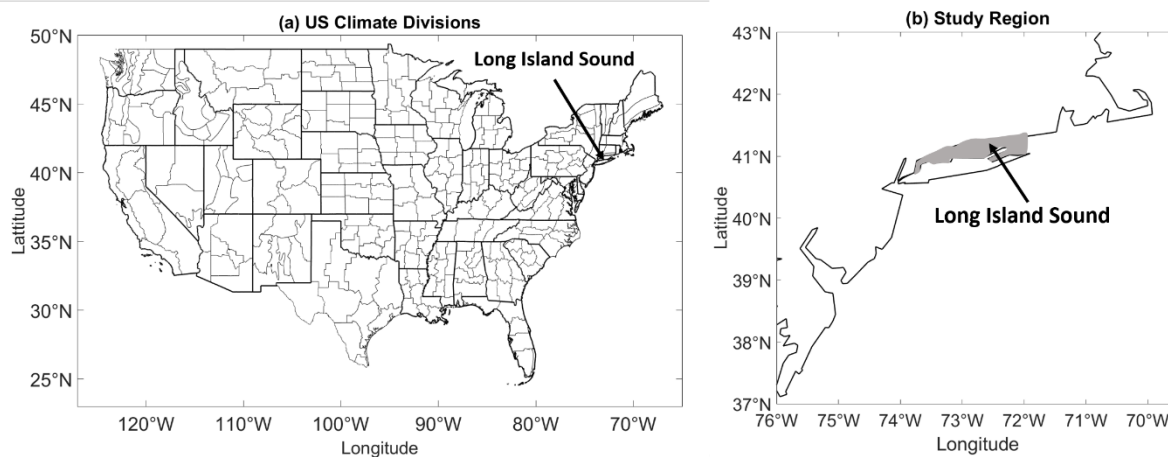


Figure 1: (a) 344 U.S climate divisions and (b) the LIS study region. Gray shading delineates the region used to calculate the LIS surface water temperature time series.

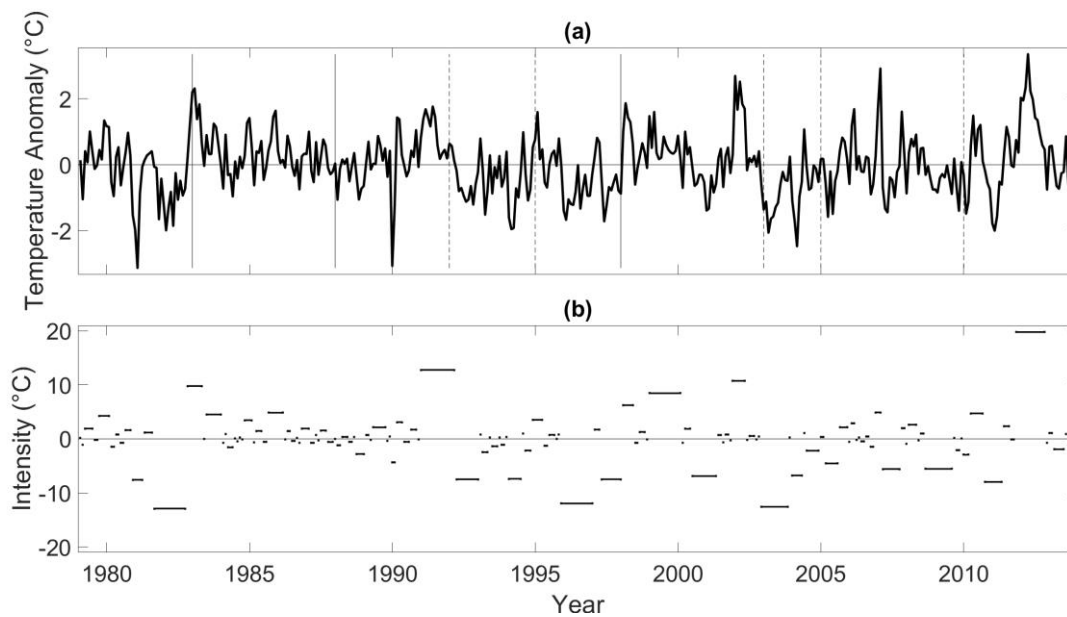


Figure 2: (a) The LIS surface temperature anomaly time series and (b) the corresponding event spectrum. The length of the line segments in (b) represents the persistence of the LIS temperature events. The vertical axis corresponds to the intensity of the event. Vertical dotted lines indicate when Central Pacific El Ninos occur and vertical solid lines indicate when Eastern Pacific El Ninos occur.

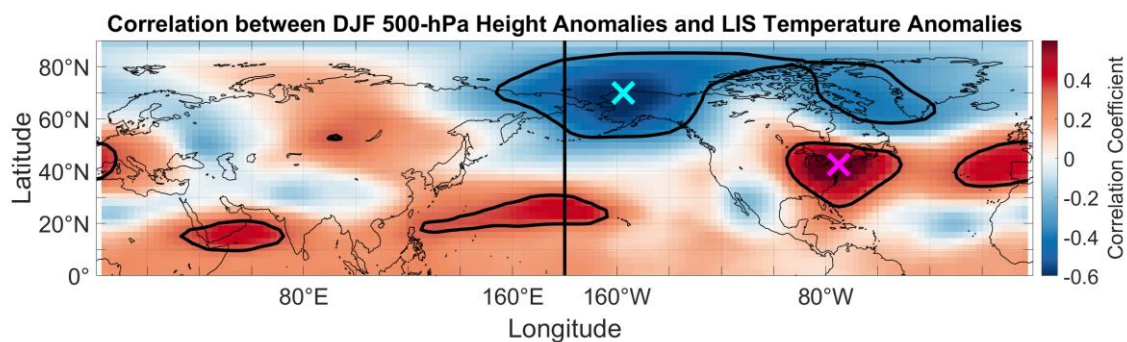


Figure 3: Correlation between DJF 500-hPa geopotential height anomalies and DJF LIS temperature anomalies. Contours enclose regions of 5% statistical significance. Crosses mark the grid point locations used to construct the dipole index.

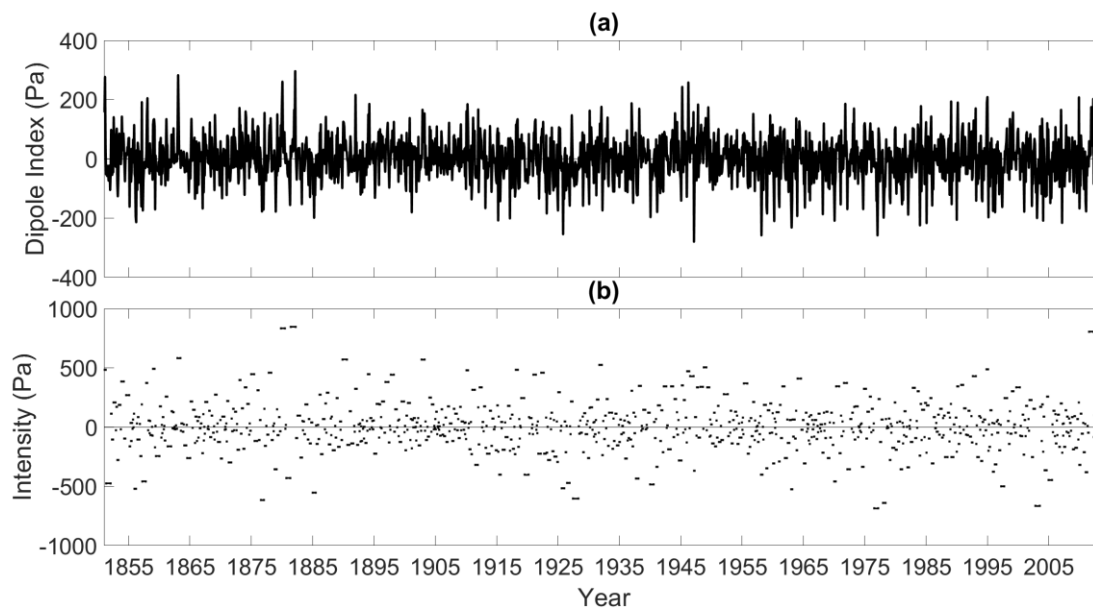


Figure 4: (a) The dipole index and (b) the corresponding event spectrum. The length of line segments in (b) represents the persistence of the dipole events. The vertical axis corresponds to the intensity of the events.

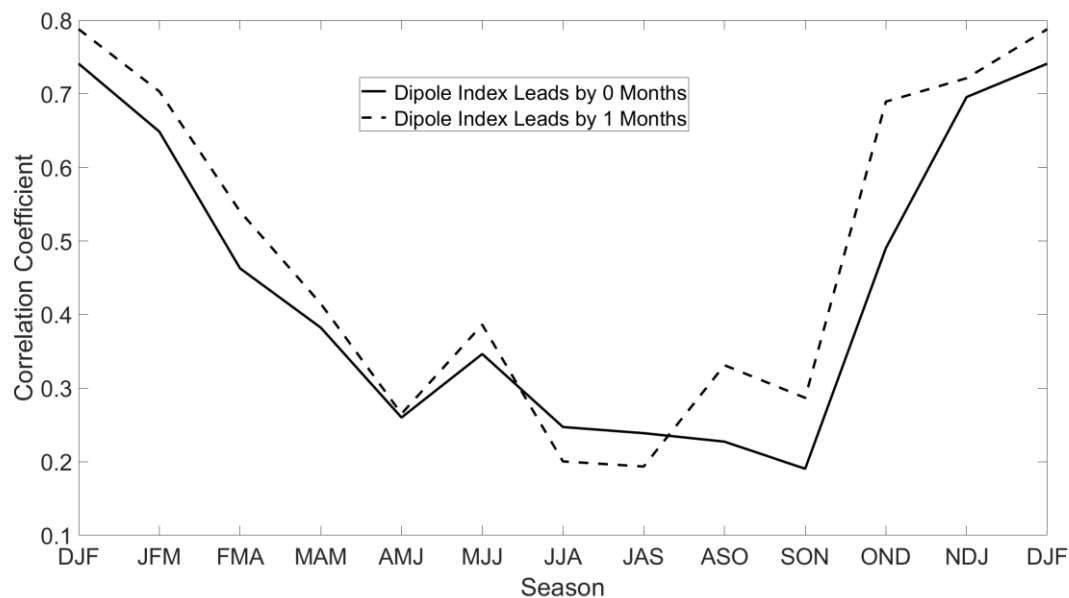


Figure 5: Lagged and simultaneous correlations between seasonally averaged LIS water temperature anomalies and the seasonally averaged dipole index. The dotted line represents the correlation between the dipole index of the prior season (dipole leads by 1 month) and water temperature anomalies for the season specified on the horizontal axis.

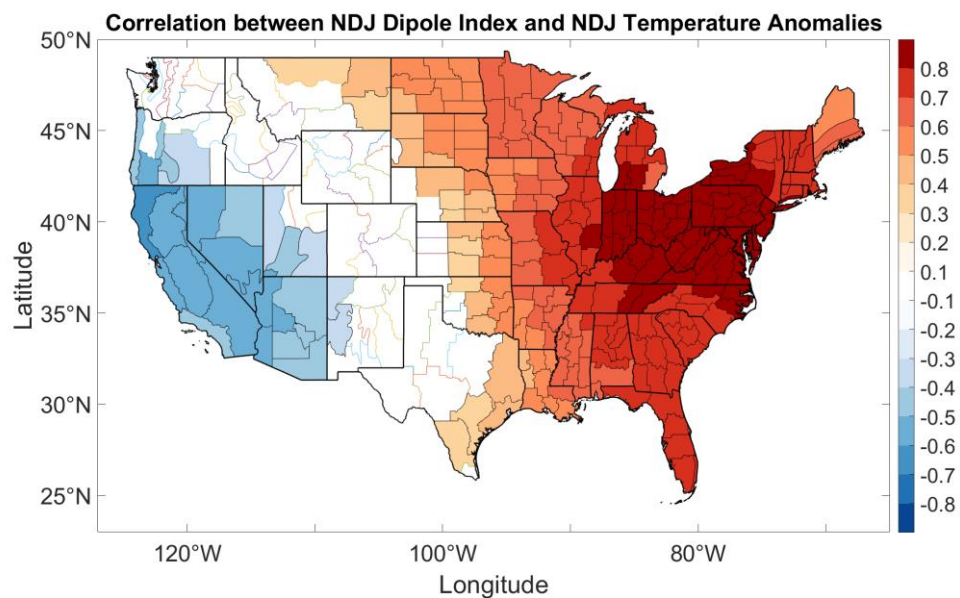


Figure 6: Correlation between the NDJ dipole index and NDJ temperature anomalies. Shaded climate divisions are those for which the corresponding correlation coefficients are statistically significant at the 5% significance level.

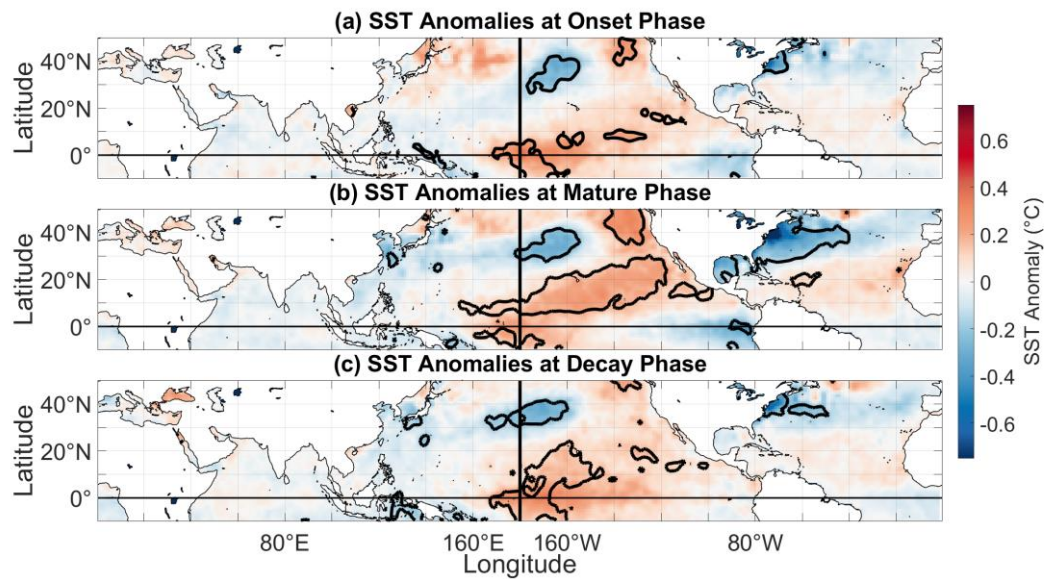


Figure 7: Composite mean SST anomalies corresponding to (a) onset, (b) mature, and (c) decay phases of negative LIS temperature events. Contours enclose regions of 5% statistical significance, as determined by a one sample *t*-test.

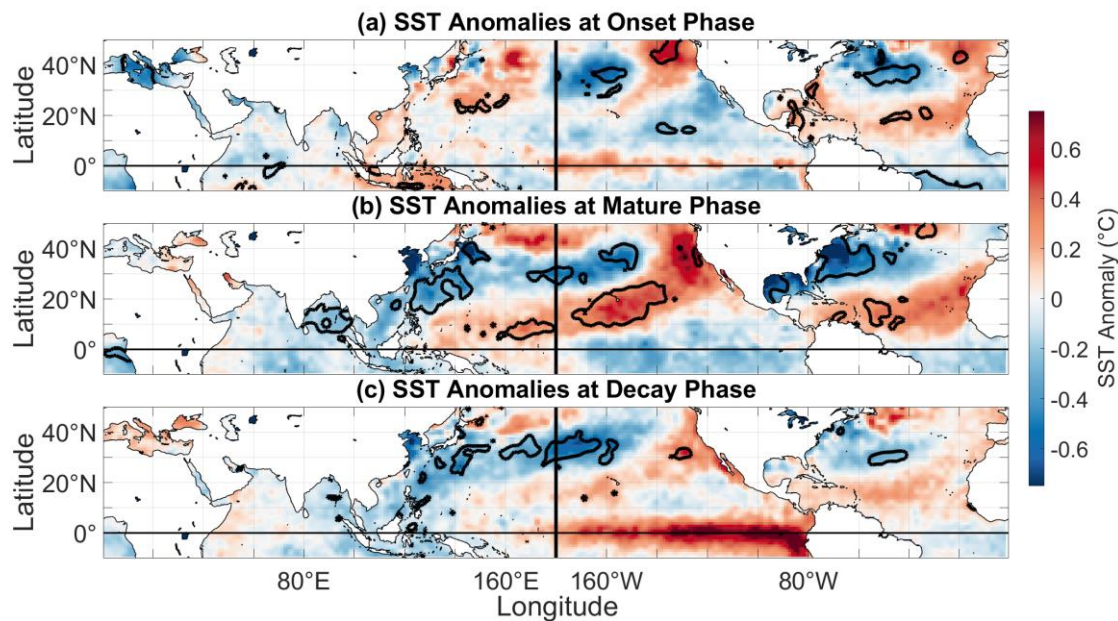


Figure 8: Same as Figure 7 but using the criterion that the LIS events fall below 1 one standard deviation from the mean intensity of all LIS cold events.

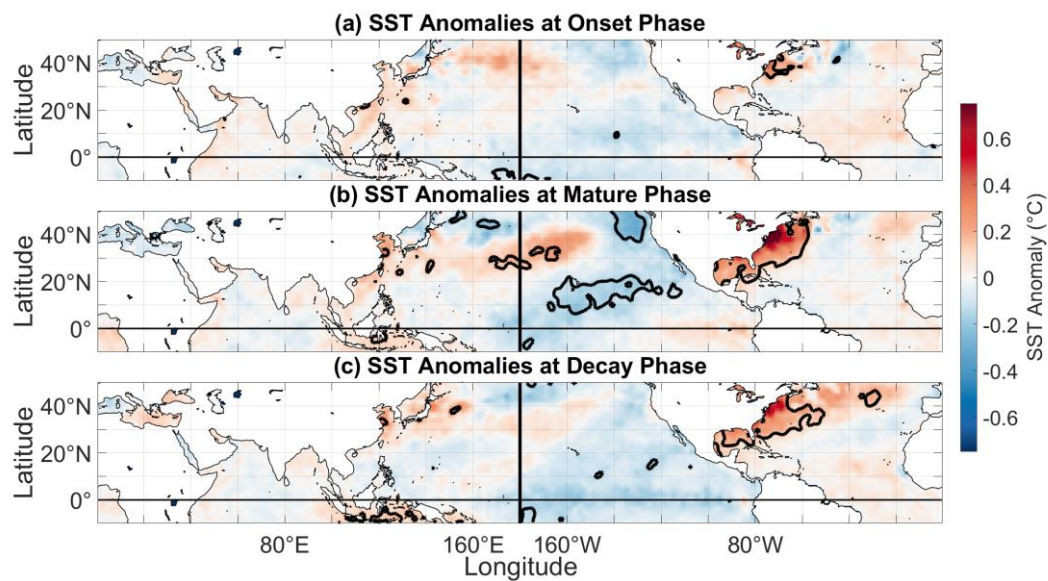


Figure 9: Same as Figure 7 except for positive LIS temperature events.

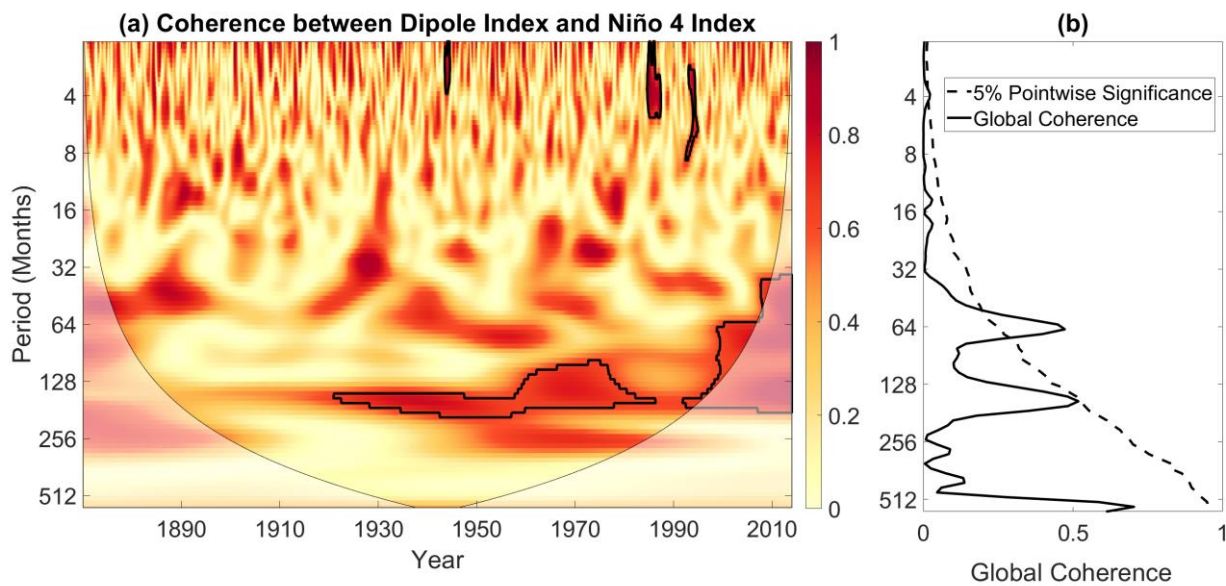


Figure 10: (a) Wavelet coherence between the dipole and Niño 4 indices. Contours enclose regions of 5% cumulative areawise significance. (b) The global coherence spectrum corresponding to (a). Dotted line is the 5% pointwise significance bound and the red curves indicate 5% arcwise significant coherence values.

5

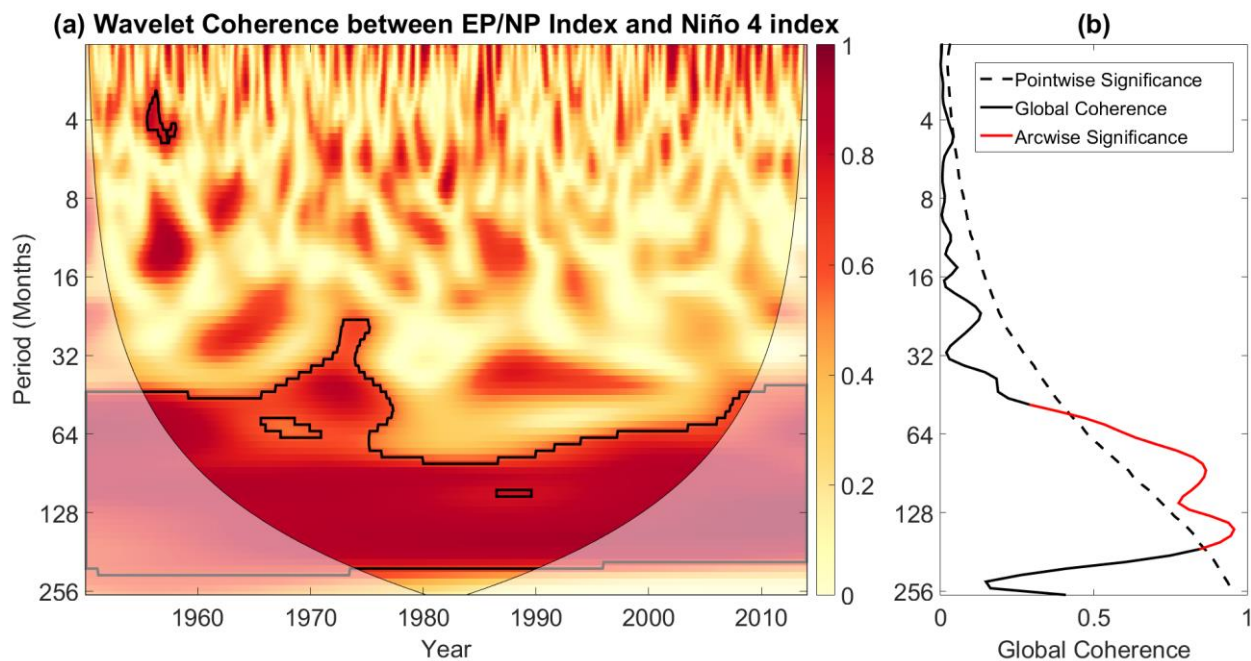


Figure 11: Same as Figure 10 but for the wavelet coherence between the EP/NP and Niño 4 indices.



Table 1. 10 LIS detrended temperature events ranked by the magnitude of their intensities.

Intensity (°C)	Persistence (Months)	Peak	Onset	Decay
20	13	March 2012	October 2011	October 2012
-13	14	January 1982	August 1981	September 1982
13	15	May 1991	December 1990	February 1992
-13	12	February 2003	November 2002	October 2003
-12	14	January 1996	November 1995	December 1996
11	6	December 2001	November 2001	April 2002
10	7	January 1983	October 1982	April 1983
9	14	February 1992	December 1998	January 2000
-8	8	January 2011	September 2010	April 2011
-8	5	January 1981	November 1980	March 1981



Table 2. 10 dipole events in the 1851-2013 period ranked by the magnitude of their intensities.

Intensity (m)	Persistence (Months)	Peak	Onset	Decay
847	11	February 1882	May 1881	March 1882
844	9	January 1880	October 1879	June 1880
805	9	March 2012	July 2011	March 2012
-687	8	January 1977	July 1976	February 1977
-666	9	January 2003	October 2002	June 2003
-638	6	January 1978	December 1977	May 1978
-616	7	September 1876	July 1876	January 1877
-604	12	August 1927	May 1927	April 1928
580	6	January 1863	December 1862	May 1863
572	9	December 1889	November 1889	July 1890



Table 3 Correlation between the dipole index and indices for 5 major climate modes of variability for the 1979-2013 period. Bold entries indicate 5% statistically significant correlation coefficients.

	J	F	M	A	M	J	J	A	S	O	N	D
EPNP	0.74	0.67	0.67	0.66	0.56	0.52	0.47	0.26	0.43	0.66	0.66	-----
WP	-0.28	-0.34	-0.19	-0.37	0.21	0.34	0.42	0.33	0.00	-0.31	-0.6	-0.56
PNA	0.29	0.0	0.0	0.0	0.35	0.12	0.12	0.46	0.43	0.30	0.15	0.0
AO	-0.6	-0.18	-0.49	-0.21	-0.52	-0.40	-0.45	-0.40	-0.37	-0.65	-0.58	-0.62
NAO	-0.59	-0.15	-0.53	-0.13	-0.50	-0.40	-0.18	-0.13	-0.1	-0.55	-0.46	-0.59



Table 4. The mode number of the EOF pattern that most closely resembles the EP/NP pattern, the explained variance associated with the EOF pattern, and the correlation coefficient, r , computed between the corresponding principal component time series and the EP/NP index. The EOF pattern that most closely resembles the EP/NP pattern was determined by finding the EOF pattern whose principal component time series is most strongly correlated with the EP/NP index. The results are based on NCEP reanalysis for the 1979-2013 period.

Quantity	J	F	M	A	M	J	J	A	S	O	N	D
r	0.66	0.66	0.61	0.62	0.67	0.44	0.51	0.60	0.63	0.69	0.61	-----
Variance (%)	14.4	5.5	3.2	5.0	7.0	1.9	4.3	5.2	4.7	6.0	4.4	-----
EOF Number	2.0	6.0	7.0	6.0	4.0	11.0	5.0	5.0	6.0	5.0	7.0	-----